

Beware of Aliases – Signal Preservation is Crucial for Robust Image Restoration

Shashank Agnihotri^{a,*}, Julia Grabinski^{a,b,c}, Janis Keuper^{c,a} and Margret Keuper^{a,d}

^aUniversity of Mannheim

^bFraunhofer ITWM, Kaiserslautern

^cInstitute for Machine Learning and Analytics (IMLA), Offenburg University

^dMax-Planck-Institute for Informatics, Saarland Informatics Campus, Saarbrücken

ORCID (Shashank Agnihotri): <https://orcid.org/0000-0001-6097-8551>, ORCID (Julia Grabinski):

<https://orcid.org/0000-0002-8371-1734>, ORCID (Janis Keuper): <https://orcid.org/0000-0002-1327-1243>, ORCID (Margret Keuper): <https://orcid.org/0000-0002-8437-7993>

Abstract. Image restoration networks are usually comprised of an encoder and a decoder, responsible for aggregating image content from noisy, distorted data and to restore clean, undistorted images, respectively. Data aggregation as well as high-resolution image generation both usually come at the risk of involving aliases, i.e. standard architectures put their ability to reconstruct the model input in jeopardy to reach high PSNR values on validation data. The price to be paid is low model robustness. In this work, we show that simply providing alias-free paths in state-of-the-art reconstruction transformers supports improved model robustness at low costs on the restoration performance. We do so by proposing *BOA-Restormer*, a transformer-based image restoration model that executes downsampling and up-sampling operations partly in the frequency domain to ensure alias-free paths along the entire model while potentially preserving all relevant high-frequency information.

1 Introduction

Computer vision, an area with tremendous advances in recent year due to improved machine learning models, is essentially a processing of 2D or 3D signals. However, in the course of modifying machine learning methods for vision tasks, some essential signal processing fundamentals have been overlooked, potentially risking unexpected model behavior. Some recent works like [18, 51, 17, 42] have explored this problem for the task of image classification. However, the remnant spectral artifacts occurring in the feature maps due to inadequate processing of signals are equally crucial for pixel-wise prediction tasks like semantic segmentation, image restoration, and others which are often involved in real-world applications that might affect human safety. Therefore, reducing these spectral artifacts is of paramount importance for a model’s reliability under noise and for model’s robustness [22]. These spectral artifacts might emerge as grid artifacts or checkerboard artifacts [34], ringing artifacts [31], or lattice artifacts [24]. Often these are visible to the human eye. However in some independently and identically distributed (i.i.d.) scenarios, the method might have learned shortcuts [13] around it, to project a sample signal from the input distribution to the target distribution.

* Corresponding Author. Email: shashank.agnihotri@uni-mannheim.de.

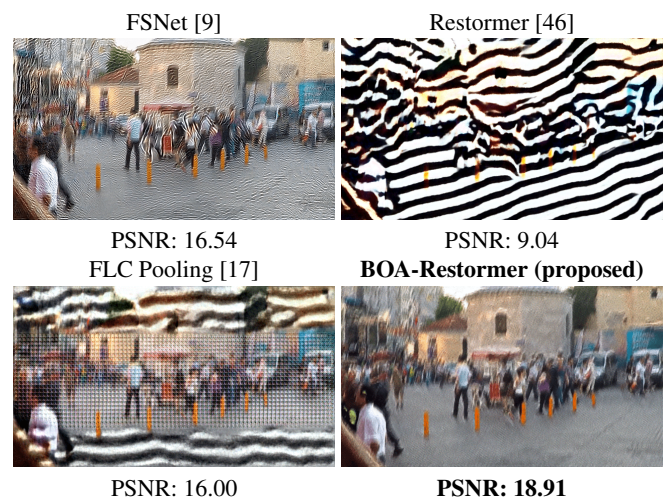


Figure 1. Comparing images deblurred by image restoration models after 10 iterations of PGD attack. We observe strong spectral artifacts in the restored images are fixed by our proposed “FrequencyPreservedPooling” (downsampling) and “FreqAvgUp” (upsampling) operations. The PSNR values reported are averaged over the entire test set.

In such scenarios, these spectral artifacts, while still existing in the learned feature representations, might not appear in the restored images and provide a wrong sense of safety. Thus, slightly perturbing the input distribution such that the perturbed and original input samples still look similar to the human eye, might help in exposing these underlying inadequately learned feature representations. Then, these would again be visible to the human eye when performing pixel-wise prediction tasks. This can be achieved by performing white-box adversarial attacks on the input images, as they optimize the perturbations by utilizing the availability of a deep neural networks (DNNs) learned weights. Therefore, we use white-box adversarial attacks to accentuate the spectral artifacts in the restored images and expose the vulnerabilities of the DNN’s learned feature representations [1]. This can be seen in Fig. 1, where FSNet [9], Restormer [46] and FLC Pooling [18] have visible artifacts under a PGD [27] attack.

Some proposed methods for vision tasks, attempt to reduce spec-

tral artifacts using low-pass filters in the Fourier domain when downsampling feature maps [17, 9, 19], motivated by the fact that convolution kernels widely used for downsampling in DNNs sample inefficiently and introduce artifacts in the learned feature representations [17]. However, depriving the DNN of the high-frequency information might have detrimental effects on tasks such as edge detection, image restoration, shape analysis, and others. One such task is image deblurring, where the blurring has already deprived the DNN of some essential high-frequency information like edges, and shapes. The restoration DNNs is expected to learn them.

Thus, in this work, we study both the downsampling and upsampling operations performed in a DNN for the image restoration task of image deblurring. We propose novel and theoretically motivated sampling methods, “FrequencyPooling” for downsampling and “FreqAvgUp” for upsampling that sample information efficiently to ensure that the artifacts in the learned representations are significantly reduced, as shown in Fig. 1.

This work makes the following contributions:

- A novel downsampling method “FrequencyPreservedPooling”, that uses the Fourier domain to downsample feature maps *without* compromising the high-frequency features and simultaneously making the network focus on low-frequency features. This increases the stability of the learned features.
- A novel upsampling method “FreqAvgUp” which uses the frequency domain, to upsample feature maps and is symmetric to “FrequencyPreservedPooling”. We refer to both modules used together as *Beware of Aliases (BOA)*-Pooling.
- The symmetry is important to allow for appropriate communication between model encoder and decoder via skip connections. We demonstrate that symmetry in the encoder and decoder helps in learning more robust representations.
- We show that focusing on low-frequency information provides samples with stable projections from the input distribution to the target distribution, leading to significantly reduced spectral artifacts in the restored images.

2 Related Work

Adversarial Robustness Adversarial robustness is a model’s robustness against intentionally crafted image perturbations that aim to fool the network. These adversarial attacks have proven to be an important tool for judging if the quality of the representations learned by a network are reasonable [3, 38, 40, 1]. While the first adversarial attacks focused on classification networks [5, 16, 27] these kinds of attacks are now broadly used on different tasks like image denoising, restoration, or semantic segmentation, to evaluate the network’s robustness [3, 21, 39]. In our work, we show that the model’s robustness can be enhanced by providing an aliasing-free path for the downsampling and upsampling in image restoration models.

Aliasing Artifacts Recent work analyzing the properties of robust models demonstrates that one important aspect of a model’s robustness is the inherent robustness against aliasing artifacts [18, 28, 48, 51]. Thereby, [48, 51] enhance a model’s shift-invariance by blurring before downsampling to reduce aliases, [28] include wavelet denoising against aliasing and for more robustness against common corruptions, [23] introduce an anti-aliasing activation function in combination with blurring before downsampling and [18] show that robust models inherently exhibit less aliasing after downsampling. While these works primarily focus on the encoding of images and

the introduced artifacts during downsampling they are equally important for upsampling methods [2]. Also in the field of image generation reducing aliasing improves the quality of the generated images [12, 25, 26].

Sampling Methods As previously discussed, aliasing artifacts arise from incorrect sampling. Thus, most work focused on the improvement of downsampling by special blurring techniques [23, 26, 28, 48, 51]. Yet, these approaches only reduce the amount of aliasing, but do not fully eliminate it. In contrast, [17, 19] propose a completely aliasing-free downsampling. However, this approach only includes the downsampling while for pixel-wise prediction tasks like image restoration upsampling is equally important. Further, all these approaches remove aliases by removing high-frequencies, the exact information that one would want to restore for beblurring. Thus, we propose a pair of down- and upsampling operations which provides the network with a completely aliasing-free path while being able to retain high-frequency information.

Upsampling is typically done via Transpose Convolution [4, 15, 29, 33, 35, 37] or Interpolation [6, 49, 50] which both suffer from spectral artifacts introduced due to incorrect sampling [2]. In Transpose Convolutions, the kernels can overlap leading to uneven contributions of the different pixels which lead to grid-like artifacts [34]. Linear interpolation can lead to aliasing artifacts which are caused by the limited context during interpolation [2].

Pixel Shuffle and Unshuffle [41] increase the spatial dimensions of the feature maps by combining r^2 channels in the Pixel Unshuffle setting and decreasing the spatial resolution of the feature maps by r in height and width to increase the channel dimension by a factor of r^2 in the Pixel Shuffle setting. Hence, the spatial resolution of the feature maps can easily be increased (upsampling) by aggregating channels or decreased (downsampling) by expanding the channel dimension while maintaining all information present in the feature maps. Yet, Pixel Unshuffle performs downsampling with sampling rate r resulting in severe aliasing artifacts [17, 19] in each channel.

All these methods are prone to spectral artifacts like aliasing. In contrast, we incorporate a way to learn high- and low-frequency information separately and thus avoid aliases in one path of our down- and upsampling method, while still incorporating the strength of Pixel Unshuffle and Pixel Shuffle in the other path.

Frequency Learning in Image Restoration Operating parts of a network in the frequency domain can enhance global information [8, 20, 36] or improve downsampling in classification tasks [17, 28]. Yet, pixel-wise prediction tasks like image restoration also apply upsampling. Thus prior work in this direction used discrete wavelet transforms to replace the up- and downsampling in a Unet [45]. Furthermore, FSNet [10] uses a multi-branch approach to select the most informative frequencies during network training and thus enhance several image restoration tasks. While [30] apply a ReLU function on the frequencies of the feature map to gain insightful information on the blur pattern in image deblurring. In MRLPFNNets [11] a low-pass filter is learned to reduce high-frequency noise and the multi-scale features from different stages of the network are fused via a wavelet-based feature fusion.

All these approaches demonstrate that changing the perspective can enhance image restoration tasks. However, all methods are driven by improvements over clean tasks while our approach is inherently more robust due to the anti-aliasing path we establish.

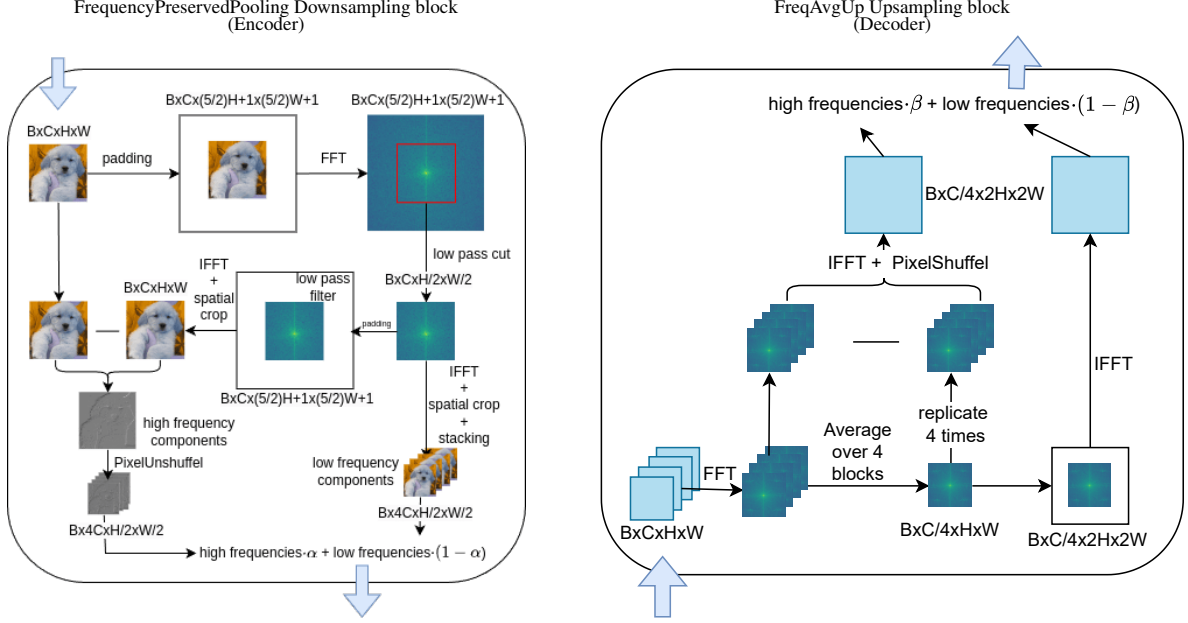


Figure 2. A visual representation of the proposed sampling operations. Left, we show the flow diagram for our proposed downsampling operation “FrequencyPreservedPooling” used in the encoder of the image restoration model’s architecture. Right, we show the flow diagram for our proposed upsampling operation “FreqAvgUp” used in the decoder of the BOA architecture.

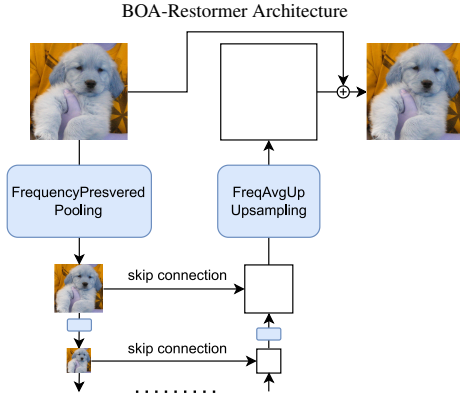


Figure 3. BOA-network architecture using our up- and downsampling from Sec. 3 and skip connections between encoder and decoder.

3 Method

We propose a method to preserve the high-frequency information while making the network also focus on low-frequency information. To this effect, we split the feature maps into their low-frequency and high-frequency components and learn the proper mixture such as to optimize the stability of the feature maps that the network learns, and to provide the network with an *alias-free* information path.

Let η_{encode} be the repeating blocks of the encoder and η_{decode} be the repeating blocks of the decoder, such that each η_{encode} is followed by a downsampling operation ζ_{down} and each decoder block is followed by an upsampling operation ζ_{up} .

Most works [46, 7] use Pixel Unshuffle [41] for downsampling and Pixel Shuffle [41] for upsampling. However, as discussed in 2, these operations can introduce artifacts in the feature maps.

Thus in our work, we modify the ζ_{down} and ζ_{up} operations in the encoder and decoder parts of the network, respectively, while keeping the encoder and decoder building blocks the same.

Following we formulate these changes. Let feature X_s of shape $[B, C, M, N]$ consist of $[x, y]_{M \times N}$ coordinates in the spatial domain, where B is the batch size, C are the number of feature channels, and the spatial resolution of the feature map is $M \times N$.

3.1 Downsampling

A naïve implementation of FLC Pooling for downsampling would not work for pixel-wise tasks such as image restoration due to the inherent nature of a low-pass filter in the Fourier domain. This generates lattice-like artifacts as shown by [24] due to Gibb’s phenomenon [14]. FLC Pooling provides good results for image classification tasks where these spectral artifacts are inconsequential. However, for image restoration tasks, since we need to preserve the locality of our signal, these artifacts have to be reduced. An ideal solution to this problem would be infinite padding, however, due to computational reasons this is not viable. Thus, we choose a more feasible padding size to reduce Gibb’s phenomenon, while keeping the size of spatial dimensions odd for additional numerical stability [19].

So, first we pad X_s on all sides such that,

$$X_{s_{B \times C \times M \times N}} \xrightarrow{\text{Padding}} X_{s_{B \times C \times \frac{M}{2} + 1 \times \frac{N}{2} + 1}} =: X_{s_{B \times C \times \bar{M} \times \bar{N}}} \quad (1)$$

Then, we obtain \hat{X}_ω by performing a 2D Discrete Fourier Transform (DFT) followed by a low pass filter on these feature maps, i.e.,

$$\hat{X}_\omega[k, l] = \frac{1}{\bar{M} \times \bar{N}} \sum_{m=0}^{\bar{M}-1} \sum_{n=0}^{\bar{N}-1} X_s[x_m, y_n] \cdot e^{-j2\pi(\frac{k}{\bar{M}}m + \frac{l}{\bar{N}}n)} \quad (2)$$

for k, l in $0, \dots, \frac{\bar{M}-1}{2}$ and $0, \dots, \frac{\bar{N}-1}{2}$, respectively. Now, $\hat{X}_\omega_{B \times C \times \frac{\bar{M}}{2} \times \frac{\bar{N}}{2}}$ are the low frequency features in $X_{s_{B \times C \times \bar{M} \times \bar{N}}}$.

Then, we zero pad \hat{X}_ω to obtain \tilde{X}_ω which is of shape $[B, C, \bar{M}, \bar{N}]$

$$\hat{X}_\omega_{B \times C \times \frac{\bar{M}}{2} \times \frac{\bar{N}}{2}} \xrightarrow{\text{Padding}} \tilde{X}_\omega_{B \times C \times \bar{M} \times \bar{N}} \quad (3)$$

Please note, Eq. (2) and Eq. (3) together represent a low-pass filter such that the threshold is the median of the frequencies present.

Then, we perform a full Inverse Discrete Fourier Transform on \hat{X}_ω to convert it to the spatial domain and obtain \tilde{X}_s

$$\hat{X}_s[m, n] = \sum_{k=0}^{\frac{M-1}{2}} \sum_{l=0}^{\frac{N-1}{2}} \hat{X}_\omega[k, l] \cdot e^{j2\pi(\frac{k}{M}m + \frac{l}{N}n)}, \quad (4)$$

and, we perform a full Inverse DFT on \tilde{X}_ω to convert it to the spatial domain and obtain \tilde{X}_s .

$$\tilde{X}_s[m, n] = \sum_{k=0}^{M-1} \sum_{l=0}^{N-1} \tilde{X}_\omega[k, l] \cdot e^{j2\pi(\frac{k}{M}m + \frac{l}{N}n)} \quad (5)$$

To emulate the increase in the number of channels done by Pixel Unshuffle operation, we then concatenate \tilde{X}_s along the C dimension four times:

$$\hat{X}_{\omega_{B \times 4C \times \frac{M}{2} \times \frac{N}{2}}} = \hat{X}_{\omega_{B \times C \times \frac{M}{2} \times \frac{N}{2}}} \parallel \hat{X}_{\omega_{B \times C \times \frac{M}{2} \times \frac{N}{2}}} \parallel \hat{X}_{\omega_{B \times C \times \frac{M}{2} \times \frac{N}{2}}} \parallel \hat{X}_{\omega_{B \times C \times \frac{M}{2} \times \frac{N}{2}}} \quad (6)$$

Next, we remove the padding from Eq. (1) in \tilde{X}_s and we obtain the features $X'_{s_{B \times C \times M \times N}}$ in the feature maps that correspond to the high frequencies in $\tilde{X}_{s_{B \times C \times M \times N}}$ using Eq. (7)

$$X'_{s_{B \times C \times M \times N}} = X_{s_{B \times C \times M \times N}} - \tilde{X}_{s_{B \times C \times M \times N}} \quad (7)$$

We downsample $X'_{s_{B \times C \times M \times N}}$ to $X'_{s_{B \times 4C \times \frac{M}{2} \times \frac{N}{2}}}$ using Pixel Unshuffle. For PixelUnshuffle, we know the information being removed, making the operation perfectly invertible. This property is crucial later when we attempt to mirror the downsampling operation, to perform an upsampling operation.

Now, we formulate the downsampling operations of the features maps, i.e. ζ_{down} as shown in Eq. (8)

$$\zeta_{down}(X_{s_{B \times C \times M \times N}}) = (1-\alpha) \cdot \tilde{X}_{s_{B \times 4C \times \frac{M}{2} \times \frac{N}{2}}} + \alpha \cdot X'_{s_{B \times 4C \times \frac{M}{2} \times \frac{N}{2}}} \quad (8)$$

where α is a learnable parameter. We learn a value for alpha such that we mix the features with low and high frequencies optimally. We initialize $\alpha=0.3$ to have a bias towards low-frequency information.

Thus, using ζ_{down} we obtain $X_{s_{B \times 4C \times \frac{M}{2} \times \frac{N}{2}}}$ which is downsampled $X_{s_{B \times C \times M \times N}}$ as shown by Eq. (9).

$$X_{s_{B \times 4C \times \frac{M}{2} \times \frac{N}{2}}} = \zeta_{down}(X_{s_{B \times C \times M \times N}}) \quad (9)$$

We name this method **FrequencyPreservedPooling (FP)**, because it allows the downsampling operation to be fully signal preserving, depending on α , while providing an alias-free path. We represent these operations as a flow diagram in Sec. 3 (left). For ablation, we also consider the scenario in which we randomly drop the high frequencies with a probability of 30%, i.e. we use only the low frequencies $\tilde{X}_{\omega_{B \times 4C \times \frac{M}{2} \times \frac{N}{2}}}$ during learning 30% of the time (batch-wise), in this scenario Eq. (8) effectively changes to

$$\tilde{\zeta}_{down}(X_{s_{B \times C \times M \times N}}) = \tilde{X}_{s_{B \times 4C \times \frac{M}{2} \times \frac{N}{2}}} \quad (10)$$

3.2 Upsampling

For upsampling the feature maps, we propose an approach symmetric to the downsampling operation. Here the objective is to perform upsampling operation ζ_{up} on $X_{s_{B \times C \times M \times N}}$ and obtain $X_{s_{B \times \frac{C}{4} \times 2M \times 2N}}$.

$$X_{s_{B \times \frac{C}{4} \times 2M \times 2N}} = \zeta_{up}(X_{s_{B \times C \times M \times N}}) \quad (11)$$

Following we describe the operations that comprise ζ_{up} .

First, we perform a DFT on the feature maps X_s that exist in the spatial domain to obtain the feature maps in the frequency domain denoted by X_ω as shown by Eq. (12).

$$X_\omega[k, l] = \frac{1}{M \times N} \sum_{m=0}^{M-1} \sum_{n=0}^{N-1} X_s[x_m, y_n] \cdot e^{-j2\pi(\frac{k}{M}m + \frac{l}{N}n)} \quad (12)$$

Since in Eq. (6) we concatenated four feature maps at a time, now we calculate \bar{X}_ω , in which replace a set of four feature maps from X_ω with average over those four feature maps along the channel dimension. This is shown by Eq. (13),

$$\bar{X}_{\omega_{B \times C \times M \times N}} = \frac{1}{4} \left(\sum_{c=0}^{c+4} X_{\omega_{B \times c \times M \times N}} \parallel \sum_{c=4}^{c+4} X_{\omega_{B \times c \times M \times N}} \parallel \dots \parallel \sum_{c=C-4}^C X_{\omega_{B \times c \times M \times N}} \right) \quad (13)$$

Please note X_ω contains both low-frequency and high-frequency information, but since during downsampling, we focus on learning low-frequency information, X_ω contains more low-frequency information and by extension same is true for \bar{X}_ω .

Next, we separate the frequencies higher than the mean to obtain X^*_{ω} for each four-tuple of channels

$$X^*_{\omega} = X_\omega - \bar{X}_\omega, \quad (14)$$

and perform IDFT on $X^*_{\omega_{B \times C \times M \times N}}$ to convert the feature maps to $X^*_{s_{B \times C \times M \times N}}$ in the spatial domain as shown by Eq. (15),

$$X^*_s[m, n] = \sum_{k=0}^{M-1} \sum_{l=0}^{N-1} X^*_{\omega}[k, l] \cdot e^{j2\pi(\frac{k}{M}m + \frac{l}{N}n)}. \quad (15)$$

This operation is followed by a Pixel Shuffle operation on $X^*_{s_{B \times C \times M \times N}}$ to upsample it to $X^*_{s_{B \times \frac{C}{4} \times 2M \times 2N}}$.

Next, we upsample $\bar{X}_{\omega_{B \times C \times M \times N}}$, by first choosing the first of every four identical channels and obtain $\bar{X}_{\omega_{B \times \frac{C}{4} \times M \times N}}$.

In Pixel Shuffle and Unshuffle, the spatial shuffle is not given. Thus, combining the 4 maps in the frequency domain is not trivial as they are shuffled in space.

Next, we are adding with zero along the x-axis and y-axis of the feature maps in the frequency domain to obtain $\bar{X}_{\omega_{B \times \frac{C}{4} \times 2M \times 2N}}$ to complete the upsampling.

This is followed by an IDFT operation on \bar{X}_ω to obtain \bar{X}_s

$$\bar{X}_s[m, n] = \sum_{k=0}^{2M-1} \sum_{l=0}^{2N-1} \bar{X}_\omega[k, l] \cdot e^{j2\pi(\frac{k}{M}m + \frac{l}{N}n)}$$

Lastly, we learn a parameter β to mix the low-frequency information and high-frequency information feature maps optimally. Thus, we express ζ_{up} by Eq. (16),

$$\zeta_{up}(X_s) = (1 - \beta) \cdot \bar{X}_s + \beta \cdot X^*_s \quad (16)$$

Here, similar to α in Sec. 3.1, we initialize β with 0.3 to induce a bias towards low-frequency information. We name this upsampling method as **FreqAvgUp**. We represent these operations as a flow diagram in Sec. 3 (right) titled ‘‘Upsampling’’.

Additionally for ablation, we explore another upsampling technique that we name **SplitUp**. Here we first, upsample the feature maps $X_{s_{B \times C \times M \times N}}$ using Pixel Shuffle to $X_{s_{B \times \frac{C}{4} \times 2M \times 2N}}$.

Then, we convert the feature maps X_s to the frequency domain using DFT and obtain X_ω similar to as shown in Eq. (12).

Next, we split the upsampled feature maps into low-frequencies \tilde{X}_ω by using a low-pass filter with the threshold being the median frequency in the feature maps, and high-frequencies \tilde{X}_ω^* by subtracting the low-frequencies from the entire feature map in the frequency domain.

Then, we convert these split feature maps to the spatial domain to obtain \tilde{X}_s (corresponds to low-frequencies) and \tilde{X}_s^* (corresponds to high-frequencies).

Lastly, we learn the parameter β to learn and mix the low-frequency and high-frequency information in the spatial domain as shown by Eq. (17), to get the upsampling operation $\tilde{\zeta}_{up}$,

$$\tilde{\zeta}_{up}(X_{s_{B \times C \times M \times N}}) = (1 - \beta) \cdot \tilde{X}_\omega + \beta \cdot \tilde{X}_s^* \quad (17)$$

Inspired by [19], to have symmetry in the Fast Fourier Transform (FFT) along the x -axis and y -axis, for every alternate downsampling and upsampling operation, we use the transposed feature maps in the spatial domain, for the FFT operation, and transpose them back to their original dimensions after having finished all operations.

4 Experiments

4.1 Experimental Setup

Following we provide the experimental setup for this work. Please refer Appendix C for additional details.

Downstream Task. We focus on the image deblurring task. We make this choice as image deblurring is a good example of a task in which preserving high-frequency information is of paramount importance, especially to restore sharp edges and object boundaries in an image, while attempting to reduce the spectral artifacts infused in the image, due to incorrect sampling. Additionally, since image deblurring is a pixel-wise task, it has an encoder and decoder in the architecture, thus helping with the study on importance of symmetry for such architectures.

Dataset. Similar to [46, 7], for our experiments we use the Go-Pro image deblurring dataset[32]. This dataset consists of 3214 real-world images, split into 2103 training images and 1111 test images, with realistic blur and their corresponding ground truth (deblurred images) captured using a high-speed camera.

Evaluation Metrics. A higher Peak Signal-to-Noise Ratio (PSNR) and a higher Structural similarity (SSIM)[44] indicate a better quality image or an image closer to the ground truth image.

Networks. For our proposed architectural design changes, we use the SotA image restoration architecture Restormer[46]. This is a Vision-Transformer based UNet-like architecture. Additionally, we compare against FSNet[9], a recently proposed image restoration model that uses Fourier transforms in their downsampling operations as well.

Adversarial Attacks. We use PGD[27] and CosPGD[3] white-box attacks as they provide a good overview of the quality of the features learned by the network[3]. As proposed by [27, 3], for both attacks we use $\epsilon \approx \frac{8}{255}$ and $\alpha=0.01$. We evaluate against these adversarial attacks over the number of iterations $\in \{5, 10, 20\}$.

4.2 Results

In the following, we discuss the experimental results from using our proposed **BOA-Restormer**, employing our downsampling method **“FrequencyPreservedPooling”** and our upsampling method **“FreqAvgUp”** for image restoration. We report the quantitative results in Tab. 1, and we provide qualitative results in Fig. 4. We provide additional qualitative results with PGD attack in Fig. 7 in Appendix B. We observe in Fig. 4, that while both Restormer and FSNet restore blurry image reasonably well, under adversarial attack Restormer’s restorations have significant visual artifacts. These visual artifacts, while reduced, also exist in the images restored by FSNet and are accentuated under strong adversarial attack (>10 attack iterations). We first ablate over naively implementing FLC Pooling[17] in the Restormer encoder for downsampling and we observe that while under attack, the spectral artifacts that exist in baseline Restormer have reduced slightly, the restored images are far from ideal and are significantly worse compared to FSNet. Additionally, due to the sinc-interpolation artifacts in FLC Pooling, we observe additional spectral artifacts in a window in the center of the images restored when using FLC Pooling for downsampling. These artifacts are called lattice artifacts by [24] and occur due to the inherent nature of low-pass filters in the Fourier domain as shown by [14]. Moreover, the images restored are still significantly blurry. We hypothesize that this is due to the removal of high-frequency information in the images, which hampers the image restoration model to restore sharp edges and image boundaries. Thus, we replace the FLC Pooling in the downsampling with **FrequencyPreservedPooling (FP)**, and observe that the spectral artifacts that existed in the restored blurry images have been removed. However, the blurry images restored under adversarial attacks still have significant spectral artifacts. Since the Restormer architecture, Restormer with FLC Pooling for downsampling and Restormer with FrequencyPreservedPooling for downsampling all use PixelShuffle for upsampling, we hypothesize that the decoder is unable to interpret the information encoded during downsampling correctly. Thus, we introduce symmetry in the downsampling-upsampling operation by replacing the PixelShuffle in “Restormer+FP” with FreqAvgUp for upsampling to obtain “BOA-Restormer”. This symmetry helps the restoration model perform significantly better, and we observe that the restored images are relatively artifacts free even under strong adversarial attacks. We discuss the importance of this symmetry in detail in Appendix A

From a quantitative perspective, in Tab. 1, we observe that the metrics reflect the observations from Fig. 4. While FSNet performs significantly better for blurry images without attack, under adversarial attacks, it lacks stability in its restorations. A similar observation is made for the baseline Restormer, which performs worse under adversarial attacks. Including FLC Pooling for downsampling, does help increase the adversarial robustness of the models. However the quality of the blurry images restored when not attacked is severely low with previously discussed spectra artifacts visible. Replacing FLC Pooling with FrequencyPreservedPooling, helps in increasing the performance of the model on blurry images when not attacked. However, it is less robust than using FLC Pooling. Lastly, we introduce symmetry in Restormer with Frequency Pooling, by replacing the upsampling operation from PixelShuffle to FreqAvgUp and observe an increase the adversarial robustness with the resulting BOA-Restormer. We observe a slight trade-off in the adversarial and non-adversarial performance, however this trade-off is expected as shown by [47, 43].

Table 1. Comparison of performance of the proposed architectural changes against CosPGD and PGD attacks with various attack strengths. Attack strength increases with the number of attack iterations (itrs). Baseline Restormer uses Pixel Unshuffle for downsampling, and Pixel Shuffle for upsampling. Thus, we first replace the Pixel Unshuffle with FLC Pooling (FLC), then we replace it with our proposed Frequency Pooling (FP). Lastly, we replace the Pixel Shuffle upsampling operation with our proposed FreqAvgUp to evaluate the full BOA-Restormer. As shown by [47, 43] a small trade-off in the adversarial and non-adversarial performance is expected .

Architecture	Test		CosPGD						PGD					
	PSNR	SSIM	5 attack itr		10 attack itr		20 attack itr		5 attack itr		10 attack itr		20 attack itr	
			PSNR	SSIM	PSNR	SSIM	PSNR	SSIM	PSNR	SSIM	PSNR	SSIM	PSNR	SSIM
FSNet[10]	33.27	0.9684	19.08	0.5184	16.51	0.3476	14.01	0.2550	19.10	0.5191	16.54	0.3485	14.08	0.2567
Restormer	31.99	0.9635	11.36	0.3236	9.05	0.2242	7.59	0.1548	11.41	0.3256	9.04	0.2234	7.58	0.1543
+ FLC	23.85	0.7811	17.3	0.4725	16.01	0.4031	14.66	0.3401	17.3	0.4723	16.00	0.4030	14.66	0.3402
+ FP	29.95	0.9395	12.17	0.3024	10.35	0.2117	9.44	0.1651	12.17	0.3018	10.35	0.2112	9.45	0.1655
BOA-Restormer (ours)	26.99	0.8806	23.9	0.7578	21.76	0.6875	21.00	0.6351	22.84	0.7290	18.91	0.6390	18.86	0.601

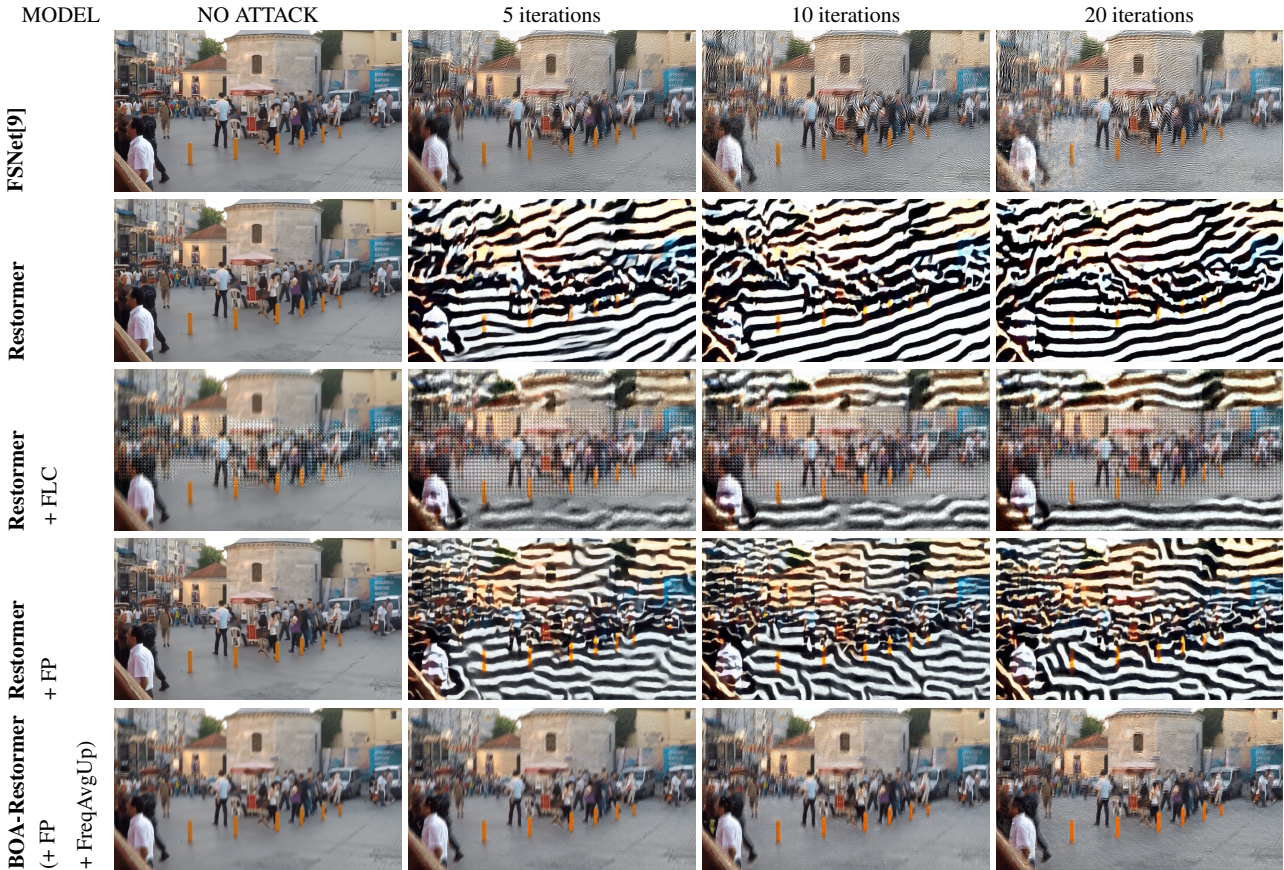


Figure 4. Comparing the proposed architectural design choices qualitatively against other baselines for image restoration, on normal blurry input images and input images adversarially attacked using CosPGD. Symbolic notations are same as those in Tab. 1.

4.3 Analysing Focus on Low-Frequencies

In the following, we ablate design decisions to encourage the focus on low-frequency information, while providing both high and low frequencies to the model. As discussed in Sec. 4.2, we observe that naïvely implementing FLC Pooling for a pixel-wise task such as image deblurring does not result in usable restored images. The better performance of “FrequencyPreservedPooling” over FLC Pooling for image deblurring indicates that retaining high-frequency information from the feature maps is crucial to the task. However, the extent to which this high-frequency information needs to be retained needs further exploration. Thus, we study “FrequencyPreservedPooling” in more detail. To this effect, we modify “FrequencyPreservedPooling”, such that for 30% of the function calls, we drop the high-frequency information, to effectively reduce “FrequencyPreservedPooling” to

Eq. (10) for these calls. We implement this ablation in two possible settings, first: allowing all downsampling steps to drop high frequencies in 30% of the calls. We denote this as “Drop High”. Second, we allow only the first downsampling step to drop high frequencies 30% of the time. We denote this as “Drop High in First Step”. The intuition behind “Drop High in First Step” is that, since the image itself might have noise that might correspond to high frequencies, reducing them to only the first downsampling step might be enough. Further reducing high-frequencies at random in all downsampling steps might deprive the model of some important information as well. We observe in Tab. 2, that this intuition is validated and indeed “Drop High in First Step” outperforms the other ablations over “FrequencyPreservedPooling”. However, when viewed qualitatively in Fig. 5, we observe a massive loss of information in the restored images,

Table 2. Different downsampling techniques compared based on performance on clean samples and performance against CosPGD and PGD attacks with various attack strengths. Baseline Restormer uses Pixel Unshuffle for downsampling. As discussed in Eq. (10) in Sec. 3.1, we ablate over dropping high frequencies during downsampling with a 30% probability. We denote this with “+ Drop High”. Additionally, we ablate over dropping high frequencies with a 30% probability only in the first downsampling step, we denote this using “+ Drop High in First Step”.

Architecture	Test		CosPGD						PGD					
	PSNR	SSIM	5 attack itrs		10 attack itrs		20 attack itrs		5 attack itrs		10 attack itrs		20 attack itrs	
			PSNR	SSIM	PSNR	SSIM	PSNR	SSIM	PSNR	SSIM	PSNR	SSIM	PSNR	SSIM
Restormer	31.99	0.9635	11.36	0.3236	9.05	0.2242	7.59	0.1548	11.41	0.3256	9.04	0.2234	7.58	0.1543
+ FLC	23.85	0.7811	17.3	0.4725	16.01	0.4031	14.66	0.3401	17.3	0.4723	16.00	0.4030	14.66	0.3402
+ FP	29.95	0.9395	12.17	0.3024	10.35	0.2117	9.44	0.1651	12.17	0.3018	10.35	0.2112	9.45	0.1655
+ FP + Drop High	29.93	0.9395	12.67	0.3707	10.34	0.2875	9.25	0.2355	12.17	0.371	10.34	0.2878	9.24	0.235
+ FP + Drop High in First Step	29.96	0.9402	13.11	0.4458	11.00	0.3513	9.75	0.2899	13.10	0.4458	10.98	0.3502	9.76	0.2907

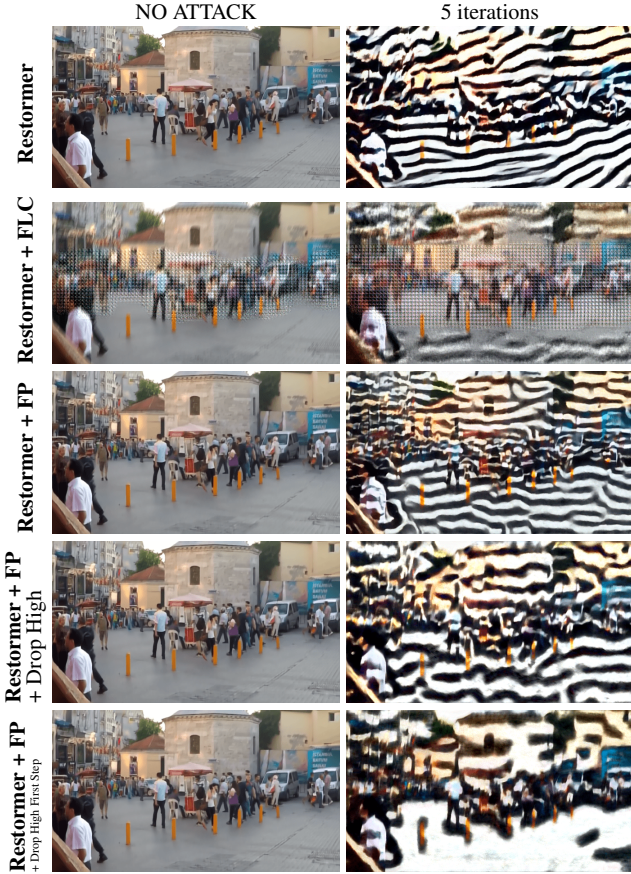


Figure 5. Different downsampling methods being compared qualitatively on normal blurry input images and input images adversarially attacked using CosPGD for five iterations. Symbolic notations are same as those in Tab. 2.

with considerable areas simply being white. Thus, for the ablations with the upsampling, we continue using “FrequencyPreservedPooling” without any explicit loss in high frequencies and do not consider its ablated variants.

Proof of Focus on Low-Frequencies. Since the proposed methods are learning a parameter for mixing the low-frequency and high-frequency information from the feature maps, we can investigate if the model is focusing on low-frequency information. We can do so by observing the values of these parameters learned for each downsampling and upsampling step. As shown in Eq. (8) and Eq. (16), a value of α and β less than 0.5 would mean the model is focusing more on low-frequency information. In Tab. 3, we report these values learned for “FrequencyPreservedPooling” and its variants. Similarly, in Tab. 4, we report the values learned for “FrequencyPreservedPool-

ing” along with the upsampling operation variants “FreqAvgUp” and “SplitUp”. For both cases, we observe that in all instances but one, the learned value for mixing the information is less than 0.5 providing strong indication for the model focusing on low-frequencies.

Table 3. Values learnt for the mixing of feature maps, α during downsampling by different downsampling operations. Restormer has three downsampling steps and thus three values of α . The initial value of α is 0.3, with the intention of inducing a bias towards low frequencies. Here the upsampling operation used is PixelShuffle. Notations “+Drop High” and “+Drop High in First Step” mean the same as in Tab. 2.

Model	α 0	α 1	α 2
Restormer + FP	0.0686	0.1703	0.0886
+ FP + Drop High	0.5239	0.2861	0.1382
+ FP + Drop High in First Step	0.1312	0.2815	0.1246

Table 4. Values learnt for the mixing of feature maps, α during downsampling and β during upsampling by different upsampling operations. Restormer has three downsampling steps and three upsampling steps, thus three values of each. The initial value of both α and β is 0.3, with the intention of inducing a bias towards low frequencies. Here the model used is “BOA Restormer”.

Upsampling Method	α 0	α 1	α 2	β 0	β 1	β 2
Freq Avg Up	0.4866	0.2805	0.2125	0.2517	0.2032	0.2246
Split Up	0.4990	0.2915	0.2281	0.2656	0.3306	0.3035

Please note, we provide an analyze the importance of symmetry in Appendix A in the Appendix.

5 Conclusion

With the increased use of machine learning in computer vision, foundational principles of signal processing are often overlooked. These foundations help guide computer vision tasks and can be utilized by machine learning methods to ensure that the model is learning meaningful representations of the data. Fortunately, for pixel-wise tasks like image deblurring, this can be validated by the human eye by spotting visible spectral artifacts in the images restored. For some scenarios, one might have to use adversarial attacks as a tool to accentuate these spectral artifacts to be visible to the human eye.

In this work, we focus on the downsampling and upsampling operations being used by some SotA architectures for image deblurring and propose more stable solutions. We propose a novel downsampling method “FrequencyPreservedPooling” and the upsampling method “FreqAvgUp” which are theoretically motivated sampling operations that lead to more stable feature representation being learned by the model without the need for adversarial training. These operations preserve important parts of the signal while discarding noise and significantly reducing all spectral artifacts in the restored images. Our final model is termed *BOA-Restormer*.

Limitations and Future Work. While, this work shows that focusing on low-frequency information, while still retaining some high-frequency information, helps the image deblurring model to restore images with significantly reduced spectral artifacts, even under adversarial attack. Yet, the performance on blurry images when not adversarially attacked is not ideal. Here, a point needs to be made for the currently used evaluation metrics that do not provide a reliable evaluation of image restoration methods, especially as they ignore spectral artifacts that are visible to the human eye. This can be observed in Fig. 1, here FLC Pooling visibly generate significantly more artifacts than FSNet, however both are very similar PSNR values. However, these metrics do serve as a community-adopted benchmark and provide some information regarding the quality of the restorations. Thus, improving our proposed methods, to perform better on these metrics like PSNR would be additionally helpful to the community.

Acknowledgements

The authors acknowledge support by the state of Baden-Württemberg through bwHPC and the German Research Foundation (DFG) through grant INST 35/1597-1 FUGG. The authors additionally acknowledge funding by the DFG Research Unit 5336 - Learning to Sense.

References

- [1] S. Agnihotri, K. V. Gandikota, J. Grabinski, P. Chandramouli, and M. Keuper. On the unreasonable vulnerability of transformers for image restoration-and an easy fix. In *Proceedings of the IEEE/CVF International Conference on Computer Vision*, pages 3707–3717, 2023.
- [2] S. Agnihotri, J. Grabinski, and M. Keuper. Improving stability during upsampling – on the importance of spatial context, 2023.
- [3] S. Agnihotri, S. Jung, and M. Keuper. CosPGD: a unified white-box adversarial attack for pixel-wise prediction tasks. In *Proceedings of the 41th International Conference on Machine Learning, ICML 2024*, 2024. URL <https://arxiv.org/abs/2302.02213>.
- [4] V. Badrinarayanan, A. Kendall, and R. Cipolla. Segnet: A deep convolutional encoder-decoder architecture for image segmentation. *TPAMI*, 39(12):2481–2495, 2017.
- [5] N. Carlini and D. Wagner. Towards evaluating the robustness of neural networks. In *2017 IEEE Symposium on Security and Privacy (SP)*, pages 39–57. IEEE, 2017.
- [6] J.-R. Chang and Y.-S. Chen. Pyramid stereo matching network. In *CVPR*, pages 5410–5418, 2018.
- [7] L. Chen, X. Chu, X. Zhang, and J. Sun. Simple baselines for image restoration. In *ECCV*, pages 17–33. Springer, 2022.
- [8] L. Chi, B. Jiang, and Y. Mu. Fast fourier convolution. In H. Larochelle, M. Ranzato, R. Hadsell, M. Balcan, and H. Lin, editors, *NeurIPS*, volume 33, pages 4479–4488, 2020.
- [9] Y. Cui, Y. Tao, Z. Bing, W. Ren, X. Gao, X. Cao, K. Huang, and A. Knoll. Selective frequency network for image restoration. In *ICLR*, 2023.
- [10] Y. Cui, W. Ren, X. Cao, and A. Knoll. Image restoration via frequency selection. *TPAMI*, 46(2):1093–1108, 2024.
- [11] J. Dong, J. Pan, Z. Yang, and J. Tang. Multi-scale residual low-pass filter network for image deblurring. In *ICCV*, pages 12345–12354, October 2023.
- [12] R. Durall, M. Keuper, and J. Keuper. Watch your up-convolution: Cnn based generative deep neural networks are failing to reproduce spectral distributions. In *CVPR*, pages 7890–7899, 2020.
- [13] R. Geirhos, J.-H. Jacobsen, C. Michaelis, R. Zemel, W. Brendel, M. Bethge, and F. A. Wichmann. Shortcut learning in deep neural networks. *Nature Machine Intelligence*, 2(11):665–673, nov 2020.
- [14] J. W. Gibbs. Fourier’s series. *Nature*, 59(200), December 1898.
- [15] I. Goodfellow, J. Pouget-Abadie, M. Mirza, B. Xu, D. Warde-Farley, S. Ozair, A. Courville, and Y. Bengio. Generative adversarial networks. *Communications of the ACM*, 63(11):139–144, 2020.
- [16] I. J. Goodfellow, J. Shlens, and C. Szegedy. Explaining and harnessing adversarial examples. 2014.
- [17] J. Grabinski, S. Jung, J. Keuper, and M. Keuper. Frequencylowcut pooling-plug and play against catastrophic overfitting. In *European Conference on Computer Vision*, pages 36–57. Springer, 2022.
- [18] J. Grabinski, J. Keuper, and M. Keuper. Aliasing and adversarial robust generalization of cnns. *Machine Learning*, pages 1–27, 2022.
- [19] J. Grabinski, J. Keuper, and M. Keuper. Fix your downsampling asap! be natively more robust via aliasing and spectral artifact free pooling, 2023.
- [20] J. Grabinski, J. Keuper, and M. Keuper. As large as it gets: Learning infinitely large filters via neural implicit functions in the fourier domain. 2023.
- [21] J. Gu, H. Zhao, V. Tresp, and P. H. Torr. Segpgd: An effective and efficient adversarial attack for evaluating and boosting segmentation robustness. In *ECCV*, pages 308–325. Springer, 2022.
- [22] J. Hoffmann, S. Agnihotri, T. Saikia, and T. Brox. Towards improving robustness of compressed cnns. In *ICML Workshop on Uncertainty and Robustness in Deep Learning (UDL)*, 2021.
- [23] M. T. Hossain, S. W. Teng, G. Lu, M. A. Rahman, and F. Sohel. Anti-aliasing deep image classifiers using novel depth adaptive blurring and activation function. *Neurocomputing*, 536:164–174, 2023.
- [24] R. Hovden, Y. Jiang, H. L. Xin, and L. F. Kourkoutis. Periodic artifact reduction in fourier transforms of full field atomic resolution images. *Microscopy and Microanalysis*, 21(2):436–441, 2015. doi: 10.1017/S1431927614014639.
- [25] S. Jung and M. Keuper. Spectral distribution aware image generation. In *AAAI*, volume 35, pages 1734–1742, 2021.
- [26] T. Karras, M. Aittala, S. Laine, E. Härkönen, J. Hellsten, J. Lehtinen, and T. Aila. Alias-free generative adversarial networks. *NeurIPS*, 34: 852–863, 2021.
- [27] A. Kurakin, I. J. Goodfellow, and S. Bengio. Adversarial machine learning at scale. In *ICLR*, 2017.
- [28] Q. Li, L. Shen, S. Guo, and Z. Lai. Wavecnet: Wavelet integrated cnns to suppress aliasing effect for noise-robust image classification. *IEEE Transactions on Image Processing*, 30:7074–7089, 2021.
- [29] J. Long, E. Shelhamer, and T. Darrell. Fully convolutional networks for semantic segmentation. In *CVPR*, pages 3431–3440, 2015.
- [30] X. Mao, Y. Liu, F. Liu, Q. Li, W. Shen, and Y. Wang. Intriguing findings of frequency selection for image deblurring. In *AAAI*, 2023.
- [31] A. Mosleh, J. M. P. Langlois, and P. Green. Image deconvolution ringing artifact detection and removal via psf frequency analysis. In D. Fleet, T. Pajdla, B. Schiele, and T. Tuytelaars, editors, *ECCV*, pages 247–262, Cham, 2014. Springer International Publishing.
- [32] S. Nah, T. H. Kim, and K. M. Lee. Deep multi-scale convolutional neural network for dynamic scene deblurring. In *CVPR*, July 2017.
- [33] H. Noh, S. Hong, and B. Han. Learning deconvolution network for semantic segmentation. In *ICCV*, pages 1520–1528, 2015.
- [34] A. Odena, V. Dumoulin, and C. Olah. Deconvolution and checkerboard artifacts. *Distill*, 1(10):e3, 2016.
- [35] A. Radford, L. Metz, and S. Chintala. Unsupervised representation learning with deep convolutional generative adversarial networks. *arXiv preprint arXiv:1511.06434*, 2015.
- [36] Y. Rao, W. Zhao, Z. Zhu, J. Lu, and J. Zhou. Global filter networks for image classification. In A. Beygelzimer, Y. Dauphin, P. Liang, and J. W. Vaughan, editors, *NeurIPS*, 2021.
- [37] O. Ronneberger, P. Fischer, and T. Brox. U-net: Convolutional networks for biomedical image segmentation. In *MICCAI*, pages 234–241. Springer, 2015.
- [38] J. Schmalzfuss, L. Mehl, and A. Bruhn. Attacking motion estimation with adversarial snow. 2022.
- [39] J. Schmalzfuss, P. Scholze, and A. Bruhn. A perturbation-constrained adversarial attack for evaluating the robustness of optical flow. In *ECCV*, pages 183–200. Springer, 2022.
- [40] S. Schrodi, T. Saikia, and T. Brox. Towards understanding adversarial robustness of optical flow networks. In *CVPR*, pages 8916–8924, 2022.
- [41] W. Shi, J. Caballero, F. Huszar, J. Totz, A. P. Aitken, R. Bishop, D. Rueckert, and Z. Wang. Real-time single image and video super-resolution using an efficient sub-pixel convolutional neural network. In *CVPR*, June 2016.
- [42] H. Sommerhoff, S. Agnihotri, M. Saleh, M. Moeller, M. Keuper, and A. Kolb. Differentiable sensor layouts for end-to-end learning of task-specific camera parameters. *arXiv preprint arXiv:2304.14736*, 2023.
- [43] D. Tsipras, S. Santurkar, L. Engstrom, A. Turner, and A. Madry. Robustness may be at odds with accuracy. In *ICLR*, 2019.
- [44] Z. Wang, A. Bovik, H. Sheikh, and E. Simoncelli. Image quality assessment: from error visibility to structural similarity. *IEEE Transactions on Image Processing*, 13(4):600–612, 2004.
- [45] H.-H. Yang and Y. Fu. Wavelet u-net and the chromatic adaptation transform for single image dehazing. In *ICIP*, pages 2736–2740, 2019.

- [46] S. W. Zamir, A. Arora, S. Khan, M. Hayat, F. S. Khan, and M.-H. Yang. Restormer: Efficient transformer for high-resolution image restoration. In *CVPR*, 2022.
- [47] H. Zhang, Y. Yu, J. Jiao, E. Xing, L. El Ghaoui, and M. Jordan. Theoretically principled trade-off between robustness and accuracy. In *ICML*, 2019.
- [48] R. Zhang. Making convolutional networks shift-invariant again. In *ICML*, 2019.
- [49] H. Zhao, J. Shi, X. Qi, X. Wang, and J. Jia. Pyramid scene parsing network. In *CVPR*, pages 2881–2890, 2017.
- [50] H. Zhao, Y. Zhang, S. Liu, J. Shi, C. C. Loy, D. Lin, and J. Jia. PSANet: Point-wise spatial attention network for scene parsing. In *ECCV*, 2018.
- [51] X. Zou, F. Xiao, Z. Yu, and Y. J. Lee. Delving deeper into anti-aliasing in convnets. In *BMVC*, 2020.

Beware of Aliases – Signal Preservation is Crucial for Robust Image Restoration

Paper #2259 Supplementary Material

A Further Analysis on Importance of Symmetry

Table 5. Different Upsampling techniques used in the decoder compared against clean performance and against CosPGD and PGD attacks with various attack strengths. Attack strength increases with the number of attack iterations (itrs). The baseline Restormer uses Pixel Shuffle for upsampling, and Pixel Unshuffle for downsampling. First we replace the downsampling operation with FrequencyPooling (FP), while still using Pixel Shuffle for upsampling. Next, we ablate over the choice of the upsampling operation by replacing PixelShuffle with SplitUp and FreqAvgUp.

Architecture	Test		CosPGD						PGD					
	PSNR	SSIM	5 attack itr		10 attack itr		20 attack itr		5 attack itr		10 attack itr		20 attack itr	
Restormer	31.99	0.9635	11.36	0.3236	9.05	0.2242	7.59	0.1548	11.41	0.3256	9.04	0.2234	7.58	0.1543
Restormer + FP	29.95	0.9395	12.17	0.3024	10.35	0.2117	9.44	0.1651	12.17	0.3018	10.35	0.2112	9.45	0.1655
+ FP + SplitUp upsampling	6.26	0.2370	6.31	0.1971	6.06	0.1854	5.79	0.1702	6.29	0.1964	6.04	0.1847	5.78	0.1697
+ FP + FreqAvgUp upsampling	26.99	0.8806	23.9	0.7578	21.76	0.6875	21.00	0.6351	22.84	0.7290	18.91	0.6390	18.86	0.601



Figure 6. Different upsampling methods being compared qualitatively on normal blurry input images and input images adversarially attacked using CosPGD. Symbolic notations are same as those in Tab. 5.

Following, we ablate over the symmetry introduced in the architecture, by making the downsampling and upsampling operations mirror images to each other. One might hypothesize, given the downsampling operation “Frequency Pooling” treats the low and high-frequency information differently, merely treating them differently again during upsampling might be enough, and performing an entirely symmetric architecture is not essential. Thus, we devise “SplitUp” as an upsampling operation, that merely splits the feature maps into low and high frequencies and learns to combine them using a learnable parameter β . However, we observe in Fig. 6, that this leads to improper sampling, causing severe artifacts in the restored images, but when under adversarial attack and not under adversarial attacks. This observation is reflected in the quantitative results reported in Tab. 5, the performance of “SplitUp” is inadequate.

B Additional Qualitative Results

Following we provide qualitative results for the models considered in Fig. 4, Fig. 6 and Fig. 5 under PGD attack and more attack iterations for Tab. 2.

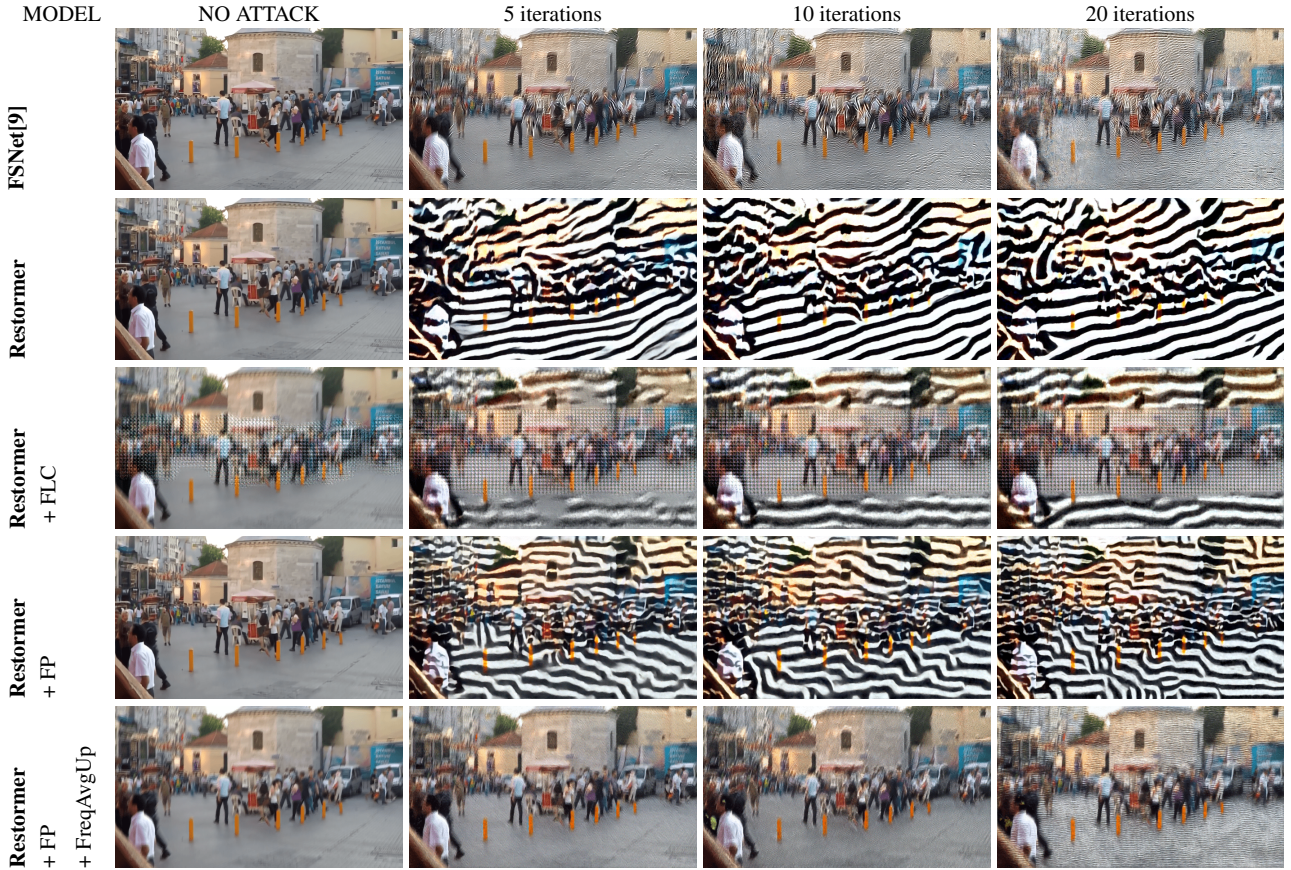


Figure 7. Comparing the proposed architectural design choices qualitatively against other baselines for image restoration, on normal blurry input images and input images adversarially attacked using PGD. Symbolic notations are same as those in Tab. 1.

C Additional Experimental Setup Details

Evaluation Metrics. We report the Peak Signal-to-Noise Ratio (PSNR) and Structural similarity (SSIM)[44] scores of the deblurred images w.r.t. to the ground truth images, averaged over all images in the test set. A higher PSNR indicates a better quality image or an image closer to the ground truth image. A higher SSIM score corresponds to better higher similarity between the two compared images.

Training Regime. To train our proposed architectures we follow the same training regime and hyperparameters as those used by [46] for training their proposed Restormer.

Compute Resources. For training and evaluation, we used a single NVIDIA A100 GPU with 48GB VRAM for each run except runs using FSNet[10]. Due to the excessive memory requirements of FSNet, for these experiments we used single NVIDIA A100 GPU with 80GB VRAM.

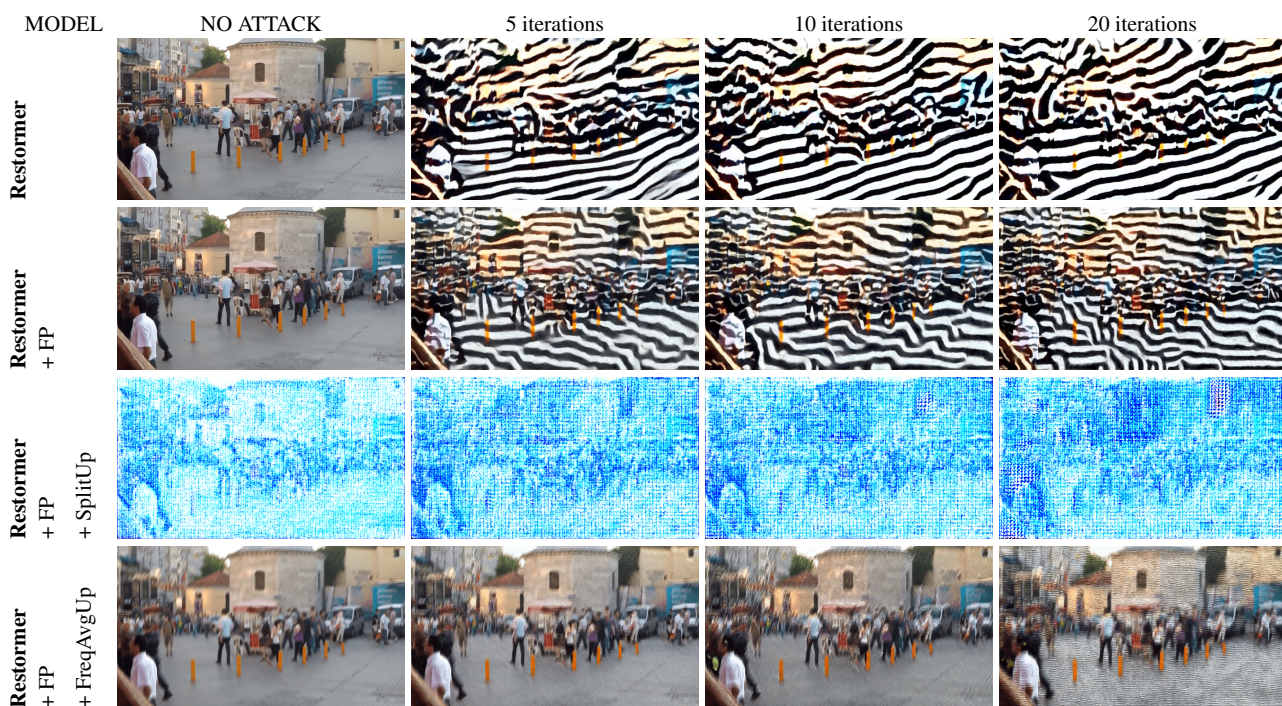


Figure 8. Different upsampling methods being compared qualitatively on normal blurry input images and input images adversarially attacked using PGD. Symbolic notations are same as those in Tab. 5.

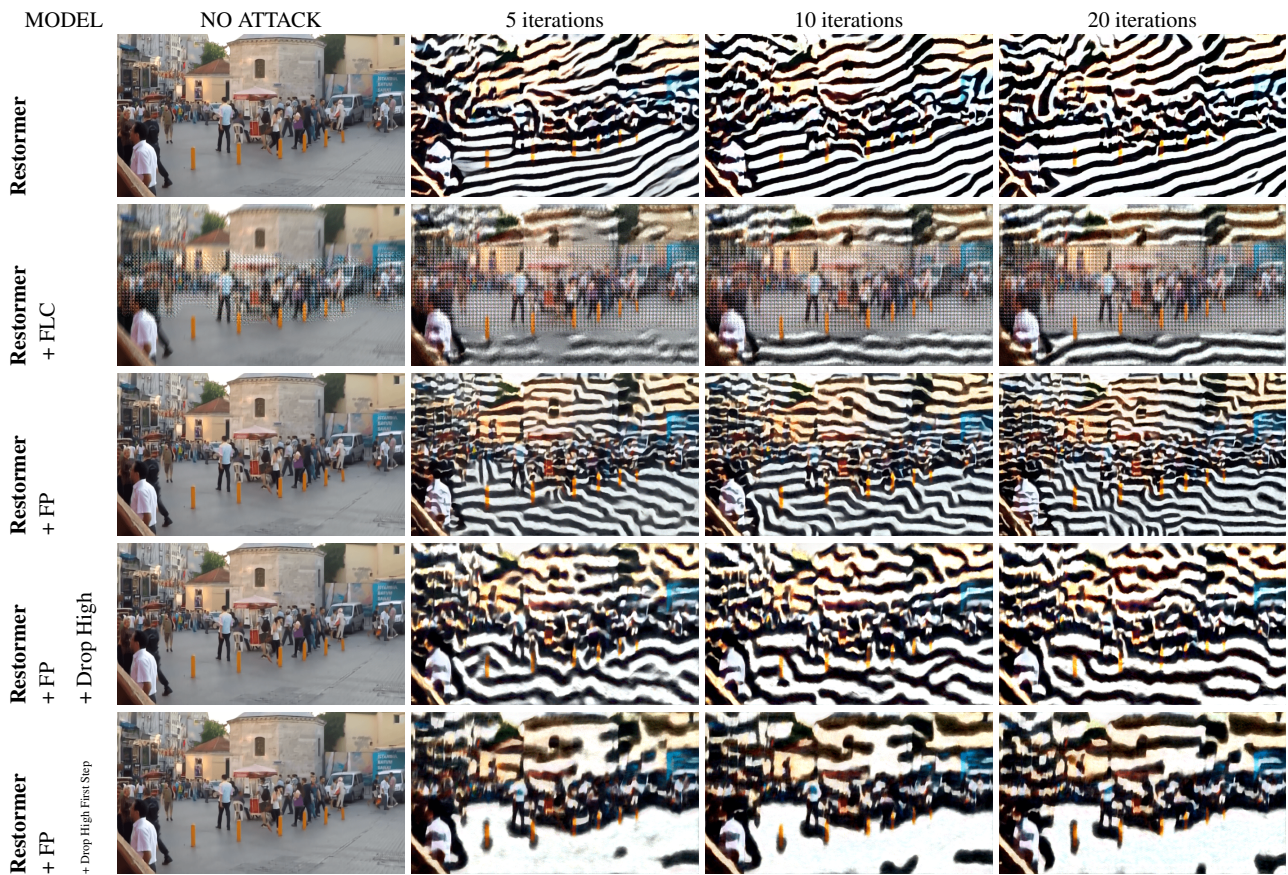


Figure 9. Different downsampling methods being compared qualitatively on normal blurry input images and input images adversarially attacked using PGD. Symbolic notations are same as those in Tab. 2.

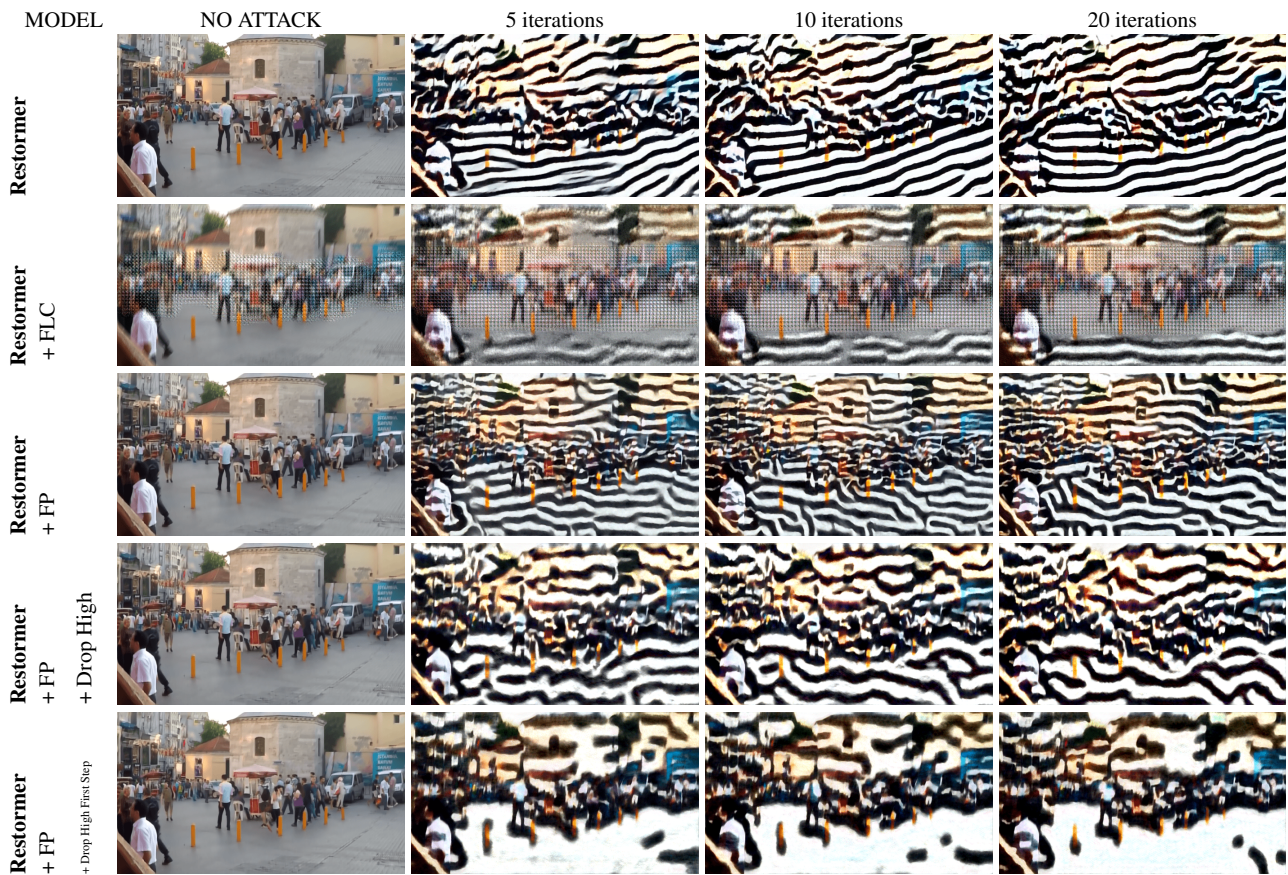


Figure 10. Different downsampling methods being compared qualitatively on normal blurry input images and input images adversarially attacked using CosPGD. Symbolic notations are same as those in Tab. 2.